Robust Anisotropic Gaussian Fitting for Volumetric Characterization of Pulmonary Nodules in Multislice CT

Kazunori Okada
Real-Time Vision and Modeling Department
Siemens Corporate Research
Princeton, NJ 08540

Dorin Comaniciu
Integrated Data Systems Department
Siemens Corporate Research
Princeton, NJ 08540

Arun Krishnan
Computer Aided Diagnosis Group
Siemens Medical Solutions
Malvern, PA 19355

Abstract

This article proposes a robust statistical estimation and verification framework for characterizing the ellipsoidal (anisotropic) geometrical structure of pulmonary nodules in the Multislice X-ray CT images. Given a marker indicating a rough location of a target, the proposed solution estimates the target's center location, ellipsoidal boundary approximation, volume, maximum/average diameters, and isotropy by robustly and efficiently fitting an anisotropic Gaussian intensity model. We propose a novel multi-scale joint segmentation and model fitting solution which extends the robust mean shift-based analysis to the linear scale-space theory. The design is motivated for enhancing the robustness against margin-truncation induced by neighboring structures, data with large deviations from the chosen model, and marker location variability. A chi-square-based statistical verification and analytical volumetric measurement solutions are also proposed to complement this estimation framework. Experiments with synthetic 1D and 2D data clearly demonstrate the advantage of our solution in comparison with the γ-normalized Laplacian approach [1] and the standard sample estimation approach [2, p.179]. A quasi real-time 3D nodule characterization system is developed using this framework and validated with two clinical data sets of thin-section chest CT images. Our experiments with 1310 nodules resulted in i) robustness against intra- and inter-operator variability due to varying marker locations, ii) 81% correct estimation rate, iii) 3% false acceptance and 5% false rejection rates, and iv) correct characterization of clinically significant non-solid (GGO) opacity nodules. This system processes each 33-voxel volume-of-interest by an average of two seconds with a 2.4GHz Intel CPU. Our solution is generic and can be applied for the analysis of blob-like structures in various other applications.

Keywords: Pulmonary nodule characterization and segmentation; Multislice X-ray CT image analysis; Part- and non-solid nodules; Anisotropic scale-space; Mean shift; Gaussian model fitting; Multi-scale analysis; Robust estimation; Covariance estimation; Chi-square verification;

1 Introduction

Lung cancer is the most common cause of cancer death in the U.S. for both sexes [3]. This makes the analysis of pulmonary nodules as one of the major issues in the computer-aided diagnosis (CAD) studies. In general, such CAD systems aim to realize i) cancer therapy monitoring and surgical follow-up examination by quantifying the volumetric change of the pathological lesions between the pre- and post-operative scans and ii) classification of malignancy/benignity of the detected pulmonary nodules. The advent of these technologies are sought for reducing the mortality rate and improving the quality of the cancer care management.

X-ray computed tomography (CT) is the most sensitive imaging domain for the pulmonary nodule analysis among others [4]. The multislice and helical CT scanners, the recent technological advances, also

greatly improved image resolution and scanning time, making the analysis of small nodules ($<$ 10 mm in diameter) feasible. Study of such small nodules is clinically important because the small tumors can still be malignant and early detection of such malignancy can drastically increase the chance of patient survival [5]. The improved image resolution indeed helps radiologists to detect nodules more accurately [6], however it also costs them more burden increasing the amount of data they need to interpret. Thus, automation of the analysis with computer-assisted systems is much needed for reducing this burden and also improving the diagnostic accuracy especially for the small nodules.

The main goal of our investigation is to solve the problem of how to best represent the nodules numerically for various analysis tasks. We refer to this problem by *nodule characterization problem*. In past decades, the technical advances in the field of computer-assisted analysis of pulmonary nodules [7, 8] have facilitated the emergence of a number of research sub-domains, such as automatic nodule detection [9, 10, 11, 12], nodule segmentation [13, 14], volume quantification [15, 16], and malignancy classification [17, 18]. The above fundamental problem cannot be avoided for realizing a solution for any of the above topics. And the solution to this problem should serve as one of the important building blocks for developing the general CAD solutions.

Within this context, this article focuses on geometrical and volumetric characterization of pulmonary nodules. We propose a comprehensive and generic computational framework based on robust multi-scale Gaussian intensity model fitting. Exploiting the model's analytical advantages, our solution provides nodule characterizations in terms of i) nodule center, ii) ellipsoidal boundary (3D segmentation approximation), iii) nodule volume, iv) maximum diameter, v) average diameter, vi) isotropy. Throughout this study, it is assumed that an observer provides a marker indicating rough location of a target lesion. This allows us to focus on the semi-automatic characterization rather than the automatic detection problem. The extension of the proposed framework to the automatic nodule detection problem is out of this article's scope but will be briefly discussed in Section 7.

1.1 Previous Work on Nodule Analysis

Automatic nodule detection is by far the most studied topic within the field of computer-assisted nodule analysis [9, 10, 11, 12, 19]. In these studies, the nodules were often characterized as spherical shapes of various size [10, 11]. However, this spherical assumption is not adequate for describing general geometry of the lesions. This is because their shape can be irregular and non-spherical due to the spiculation or the

attachments to the pleural surface (i.e., juxtapleural and peripheral) and to the vessels (i.e.,vascularized) [14].

For characterizing nodules in 3D CT data, the *tumor size or volume* is most intuitive and the well-established method [4, 7]. Such underlining scales of lesions provide important clinical information, enabling to measure the *tumor growth* that correlates highly with probability of malignancy. The recent approaches for the tumor size estimation can be roughly categorized into segmentation- and model-based methods. The segmentation-based methods are based on delineation of the voxels belonging to the nodules by using voxel intensity thresholding. For instance, in their study for quantifying growth-rate of nodules, Kostis et al. [14] characterized different types of nodules by segmenting them based on the intensity thresholding followed by the morphological operations. On the other hand, the model-based methods describes nodules by fitting geometrical or intensity models to the data. For the pulmonary nodules, the model describing voxel intensity distribution in the 3D data space is preferred to the one representing geometry of 3D tumor boundary (e.g., deformable contour model [20]), because the intensity distribution conveys more information than the tumor boundary which may be ill-defined for a certain type of nodules [21]. The most common approach for the model-based methods is the template matching of isotropic Gaussian intensity templates [10, 11]. For instance, Lee et al. [10] developed a system for automatic nodule detection by using four different sizes of spherical nodule templates in their genetic algorithm-based template matching technique.

For volume quantification, the segmentation-based approaches have often been employed due to their capability to handle irregular geometry. In practice, however, it is difficult to achieve high volume estimation accuracy due to the intrinsic uncertainty of the voxel values caused by different scanner settings as well as the non-solid opacities of the tumor boundary. On the other hand, the model-based approaches may be more rigid but they can also incorporate a variety of statistical methods for improving the estimation accuracy (e.g., Markov random field [11], non-parametric density analysis [12]).

1.2 Our Approach

Robustness is one of the key issues addressed in this article. We seek a nodule characterization solution that is robust against the characteristics of the real CT data with noise which is intrinsic to the measurement process and also the pathology and anatomy of our interest. For example, a recent clinical study suggested that the part- and non-solid or ground-glass opacity nodules, whose intensity distribution is largely irregular, are more likely to be malignant than solid ones [21]. Despite this clinical demand, to our best knowledge,

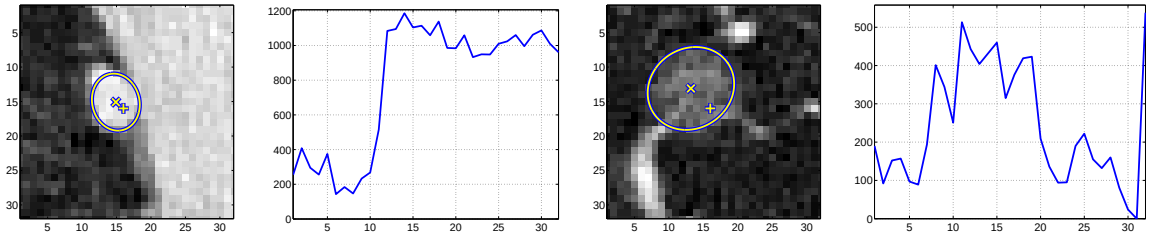

(a) **(b)** **(c)** **(d)**

Figure 1: An illustration of pulmonary nodule examples with typical data noises captured in 3D CT images. From left to right, (a): nodule attached to pleural surface in 2D dissection, (b): 1D horizontal profile of (a) through the nodule center, (c): non-solid vascularized nodule, and (d): 1D vertical profile of (c). The voxel-intensities in (b,d) indicate the Hounsfield unit with an offset 1024. "+" denotes markers used as initialization points provided by expert radiologists. The estimated nodule center and anisotropic spread are shown by "x" and 35% confidence ellipses, respectively.

no comprehensive solutions for detecting, segmenting, and/or characterizing these difficult cases have been proposed. Fig.1 illustrates examples of such difficult cases. The figure shows 2D dissections and 1D profiles of the two lesions for the juxtapleural [14] and non-solid nodules. In developing an algorithm to describe them, our solution must be robust against:

1. influences from surrounding structures such as the pleural surface and vessels (i.e., margin-truncation: Fig.1a,b),
2. deviation of the signal from a Gaussian intensity model of our choice (i.e., non-Gaussianity: Fig.1c,d), and
3. uncertainty in the marker location + given by system users (i.e., initialization: Fig.1a,c).

In another words, we seek a method that estimates the nodule boundary (shown by the solid-line ellipses around the center **x** in the figure) and its volumetric measurements even with the presence of these problems.

The proposed framework consists of three successive stages: i) model estimation, ii) model verification, iii) volumetric measurements. As our solution to the model estimation problem, this article presents a novel statistical framework for robust multi-scale joint segmentation and model fitting. Addressing the issues discussed in the previous section, our solution utilizes the model-based approach. The anisotropic (non-spherical) Gaussian function is chosen as our intensity model. Such anisotropic Gaussian captures the 3D nodule center by its mean location and the 3D anisotropic spread (i.e., shape and orientation of an ellipsoid) by its fully-parameterized covariance matrix, making our model more flexible than the spherical one.

Our multi-scale analysis is driven by Gaussian scale-space [22, 23] over a set of discrete analysis scales given *a priori*. For each scale, we estimate the Gaussian mean and covariance that fits best to the corresponding scale-space image, resulting in a set of the mean and covariance estimates. In order to choose the best fit among this set, a stability test is performed by evaluating Jensen-Shannon divergence over the analysis scales. The estimate with the minimum divergence corresponds to the most stable estimate and serves as the best fit.

At a specific scale, the mean and covariance are estimated by using a novel mean shift-based analysis. This article presents a formal extension of the mean shift analysis to the Gaussian scale-space by unifying the robust statistical methods for density gradient estimation [24] and continuous linear scale-space theory [22, 23, 1]. By likening the arbitrary positive function describing an image signal to the probability density function, the density mean shift-based analysis is extended towards the Gaussian model fitting in the continuous function domain. The resulting scale-space mean shift defines a convergent gradient-ascent in the Gaussian scale-space image, as well as the basin of attraction of a target tumor. Using this scale-space mean shift, the mean is estimated by the convergence of majority of initial points sampled around the marker location. The covariance is estimated by solving a set of linear equations constructed with mean shift vectors convergent to the estimated mean. We present a closed-form analytical solution to this least-squares problem with the symmetric positive definite constraint. The joint segmentation and model fitting is achieved for the mean and covariance estimations by using only convergent mean shift vectors, ignoring the non-convergent mean shifts as outliers and exploiting inlier statistics only from the basin of attraction of the target tumor.

The robustness of this framework is facilitated by a number of factors. The stability criterion used for scale (bandwidth) selection facilitates the robustness against the non-Gaussianity because it does not depend on specific error measures of ill-fitting. This should enable our solution to handle part- and non-solid nodule cases with high non-Gaussianity. The joint segmentation and model fitting approach facilitates the robustness against the margin-truncation because information from the non-target neighboring structures can be ignored by treating them as outliers. This should help to fit the model correctly with the cases surrounded by vessels or pleural surfaces. The scale-space mean shift-based covariance estimation also mitigates the initialization variation because a set of inliers used for the least-squares do not depend on specific initializations, leading to low intra- and inter-operator variability with varying marker locations.

For the model verification problem, a statistical verification method based on chi-square analysis is also proposed to complement the robust estimation framework. One of the advantages of our statistical ap-

proach is the availability of such goodness-of-fit measures that provide information of how well the resulting statistical estimates and the specific model function fit to the data. In practice, such measures are of extreme importance, enabling to reject accidental ill-estimates.

Once the model estimation and verification stages are performed, the approximation of the 3D nodule boundary segmentation is provided as the confidence ellipsoid of the fitted Gaussian with a specific limit of probability mass, forming a 3D equal-probability contour. Such an ellipsoid can be used an intuitive visualization of the 3D nodule shapes. Consequently, the volumetric measurements of the target nodule are derived from the volumetry of the confidence ellipsoid. We propose closed-form analytical solutions for measuring the volume, maximum and average diameter, and isotropy in a physical unit as a function of eigenvalues and eigenvectors of the estimated covariance matrix. The proposed solutions inherit the robustness of the Gaussian fitting process, facilitating low intra- and inter-operator variability. On the other hand, we have recently developed a non-parametric 3D tumor segmentation solution which employs the Gaussian model fitted by the proposed method as a prior [25]. Such a solution enables more accurate volume measurement than the proposed ellipsoidal approach, however, the analytical nature of the presented solution provides the type of measurement, such as average diameter and isotropy, that are difficult to obtain by using the conventional segmentation or manual methods.

1.3 Related Work

There are a number of techniques in the literature that are related to our proposed method. In general, Gaussian model fitting is a well-studied standard technique [26, ch.2]. It is, however, not trivial to fit such a model to data with outliers and margin-truncation induced by neighboring structures. For example, minimum volume ellipsoid covariance estimator [27] addresses the robustness to the outliers however its effectiveness is limited regarding the truncation issue.

Bahalerao and Wilson [28] proposed an intensity model fitting method applied for visualizing 3D vascular structures in MR images. They utilized anisotropic model similar to ours, however their method does not exploit the robust statistics and involves an expensive EM algorithm-based iterative solution for the model fitting. Our proposed method exploits a closed form algebraic solution, making it more efficient.

Despite the seminal work by Perona and Malik [29], the extension of the Gaussian scale-scale theory to the anisotropic analysis kernel has not been thoroughly studied for its application towards non-edge feature extraction. Manmatha and Srimal [30] developed a hand writing segmentation system utilizing an

anisotropic scale-space-based blob detection technique. However, they considered anisotropy only up to a diagonal covariance matrix. The extension to the full anisotropy along arbitrary axis is provided by our solution. Robust anisotropic diffusion proposed by Black et al. [31] addresses the exploitation of the robust statistics within the anisotropic diffusion paradigm. Although we share the same motivation towards the robust estimation, the resulting method is not directly related to ours and not applicable to our problem. Finally, to our knowledge, there are no pulmonary tumor analysis systems reported in the literature, which employ the robust estimation methods for describing the ellipsoidal tumor structure and for deriving volumetric measurements from the fitted ellipsoid.

1.4 Organization

This article is organized as follows. The proposed methods are described in the next three sections. Sections 2 3 and 4 formally describe the proposed model fitting, model verification, and volumetric measurement methods, respectively. An overview of the proposed algorithm is given in Section 5. Section 6 provides the results of our experiments. The robustness of the proposed methods is empirically studied with synthetic data and the results are described in Section 6.1. The nodule analysis system based on the proposed framework is evaluated in Section 6.2. This article is concluded by discussing our findings and future work in Section 7.

2 Robust Multi-Scale Gaussian Model Fitting

This section presents the robust parameter estimation for the multi-scale Gaussian-based model fitting as a solution for characterizing 3D nodule boundary. In the following, the terms *mean* and *covariance* are used interchangeably with *spatial local maximum* and *spread*, respectively.

2.1 Gaussian-based Intensity Model

The pulmonary nodule in a chest CT image typically appears as a local concentration of high CT values surrounded by very low CT values of lung parenchyma as background. One of the most common model functions for describing the characteristics of such bounded signals is the Gaussian function.

We treat the volumetric CT image as the discretization of a d(=3)-dimensional continuous non-negative signal $f(\mathbf{x})$ over a 3D regular lattice. The non-positiveness is assured by using the offset with

1024 to the CT values in Hounsfield unit. The symbol $\mathbf{u}$ is used for describing the location of a spatial local maximum of f (or a mode in the sense of density estimation). Suppose that the local region of f around $\mathbf{u}$ can be approximated by a product of a d-variate Gaussian function and a positive multiplicative parameter,

$$f(\mathbf{x}) \simeq \alpha \times [\Phi(\mathbf{x}; \mathbf{u}, \mathbf{\Sigma})]_{\mathbf{x} \in \mathcal{S}} \quad (1)$$

$$\Phi(\mathbf{x}; \mathbf{u}, \mathbf{\Sigma}) = (2\pi)^{-d/2} |\mathbf{\Sigma}|^{-1/2} \exp(-\frac{1}{2}(\mathbf{x}-\mathbf{u})^t \mathbf{\Sigma}^{-1}(\mathbf{x}-\mathbf{u})) \quad (2)$$

where $\mathcal{S}$ is a set of data points in the neighborhood of $\mathbf{u}$, belonging to the basin of attraction of $\mathbf{u}$. An alternative is to consider a model with a DC component $\beta \geq 0$ so that $f \simeq \alpha \times \Phi + \beta$. It is, however, straightforward to locally offset the DC component. Thus we will not consider it within our estimation framework favoring a simpler form. Later, we will revisit this extended model for the statistical verification of the resulting estimates. The problem of our interest can now be understood as the parametric model fitting and the estimation of the model parameters: mean $\mathbf{u}$, covariance $\mathbf{\Sigma}$, and amplitude α. The *mean* and *covariance* of Φ describe the *spatial local maximum* and *spread* of the local structure, respectively. The anisotropy of such structure can be specified only by a fully-parameterized covariance.

2.2 Anisotropic Scale-Space Representation

The scale-space theory [22, 23, 1] states that, given any d-dimensional continuous signal $f : \mathcal{R}^d \rightarrow \mathcal{R}$, the scale-space representation $F : \mathcal{R}^d \times \mathcal{R}_+ \rightarrow \mathcal{R}$ of f is defined to be the solution of the diffusion equation, $\partial_h F = 1/2 \nabla^2 F$, or equivalently the convolution of the signal with Gaussian kernels $\Phi(\mathbf{x}; \mathbf{0}, \mathbf{H})$ of various bandwidths (or scales) $\mathbf{H} \in \mathcal{R}^{d \times d}$,

$$F(\mathbf{x}; \mathbf{H}) = f(\mathbf{x}) * \Phi(\mathbf{x}; \mathbf{0}, \mathbf{H}). \quad (3)$$

When $\mathbf{H} = h\mathbf{I}$ ($h > 0$), F represents the solution of the isotropic diffusion process [1] and also the Tikhonov regularized solution of a functional minimization problem, assuming that scale invariance and semi-group constraints are satisfied [32]. When $\mathbf{H}$ is allowed to be a fully-parameterized symmetric positive definite matrix, F represents *anisotropic scale-space* * that is the solution to a partial differential equation: $\partial_{\mathbf{H}} F = 1/2 \nabla \nabla^t F$.

*This is different from the well-known anisotropic diffusion [29] that is with the inhomogeneous, thus spatially dependent, bandwidth $\mathbf{H}(\mathbf{x})$.

2.3 Mean Shift Procedure for Continuous Scale-Space Signal

In this section, we extend the fixed-bandwidth mean shift [33], introduced previously for the non-parametric point density estimation, towards the analysis of continuous signal evaluated in the linear scale-space.

The gradient of the scale-space representation $F(\mathbf{x};\mathbf{H})$ can be written as convolution of f with the Gaussian derivative kernel $\nabla\Phi$, since the gradient operator commutes across the convolution operation. Some algebra reveals that ∇F can be expressed as a function of a vector whose form resembles the density mean shift,

$$\begin{aligned}
\nabla F(\mathbf{x};\mathbf{H}) &= f(\mathbf{x}) * \nabla\Phi(\mathbf{x};\mathbf{H}) \\
&= \int f(\mathbf{x}')\Phi(\mathbf{x}-\mathbf{x}';\mathbf{H})\mathbf{H}^{-1}(\mathbf{x}'-\mathbf{x})d\mathbf{x}' \\
&= \mathbf{H}^{-1}\int \mathbf{x}'\Phi(\mathbf{x}-\mathbf{x}';\mathbf{H})f(\mathbf{x}')d\mathbf{x}' - \mathbf{H}^{-1}\mathbf{x}\int \Phi(\mathbf{x}-\mathbf{x}';\mathbf{H})f(\mathbf{x}')d\mathbf{x}' \\
&= \mathbf{H}^{-1}F(\mathbf{x};\mathbf{H})\mathbf{m}(\mathbf{x};\mathbf{H}) \qquad (4) \\
\mathbf{m}(\mathbf{x};\mathbf{H}) &\equiv \frac{\int \mathbf{x}'\Phi(\mathbf{x}-\mathbf{x}';\mathbf{H})f(\mathbf{x}')d\mathbf{x}'}{\int \Phi(\mathbf{x}-\mathbf{x}';\mathbf{H})f(\mathbf{x}')d\mathbf{x}'} - \mathbf{x}. \qquad (5)
\end{aligned}$$

Eq.(5) defines the extended fixed-bandwidth mean shift vector for f. Setting $f(\mathbf{x}') = 1$ in Eq.(5) results in the same form as the density mean shift vector. Note however that $\mathbf{x}$ in Eq.(5) is an ordinal variable while a random variable was considered in [33]. Eq.(5) can be seen as introducing a weight variable $w \equiv f(\mathbf{x}')$ to the kernel $K(\mathbf{x}') \equiv \Phi(\mathbf{x}-\mathbf{x}')$. Therefore, an arithmetic mean of $\mathbf{x}'$ in our formulation of mean shift is not weighted by the Gaussian kernel but by its product with the signal $K'(\mathbf{x}') \equiv \Phi(\mathbf{x}-\mathbf{x}')f(\mathbf{x}')$.

The mean shift procedure [24] is defined as iterative updates of a data point $\mathbf{x}_i$ until its convergence at $\mathbf{y}_i^m$,

$$\mathbf{y}_{j+1} = \mathbf{m}(\mathbf{y}_j;\mathbf{H}) + \mathbf{y}_j; \quad \mathbf{y}_0 = \mathbf{x}_i. \qquad (6)$$

Such iteration gives a robust and efficient algorithm of gradient-ascent, since $\mathbf{m}(\mathbf{x};\mathbf{H})$ can be interpreted as a normalized gradient by rewriting Eq.(4); $\mathbf{m}(\mathbf{x};\mathbf{H}) = \mathbf{H}\nabla F(\mathbf{x};\mathbf{H})/F(\mathbf{x};\mathbf{H})$. F is strictly non-negative valued since f is assumed to be non-negative. Therefore, the direction of the mean shift vector aligns with the exact gradient direction when $\mathbf{H}$ is isotropic with a positive scale.

2.4 Robust Spatial Local Maxima Estimation

We assume that the data is given with information of where the target structure is roughly located but we do not have explicit knowledge of its spread. The marker point $\mathbf{x}_p$ indicates such location information. We

allow $\mathbf{x}_p$ to be placed anywhere within the basin of attraction $\mathcal{S}$ of the target structure. To increase the robustness of this approach, we run N_1 mean shift procedures initialized by sampling the neighborhood of $\mathbf{x}_p$ uniformly. The majority of the procedure's convergence at the same location indicates the location of the maximum. The point proximity is defined by using the Mahalanobis distance with $\mathbf{H}$. This approach is efficient because it does not require the time-consuming explicit construction of $F(\mathbf{x};\mathbf{H})$ from $f(\mathbf{x})$.

2.5 Robust Anisotropic Covariance Estimation by Constrained Least-Squares in the Basin of Attraction

In the sequel we estimate the fully-parameterized covariance matrix $\mathbf{\Sigma}$ in Eq.(1), characterizing the d-dimensional anisotropic spread and orientation of the signal f around the local maximum $\mathbf{u}$. Classical scale-space approaches relying on the γ-normalized Laplacian [1] are limited to the isotropic case thus not applicable to this problem. Another approach is the standard sample estimation of $\mathbf{\Sigma}$ by treating f as a density function [2, p.179]. However, this approach becomes suboptimal in the presence of the margin-truncations. Addressing this issue, we present a constrained least-squares framework for the estimation of the anisotropic fully-parameterized covariance of interest based on the mean shift vectors collected within the basin of attraction of $\mathbf{u}$.

With the signal model of Eq.(1), the definition of the mean shift vector of Eq.(5) can be rewritten as a function of $\mathbf{\Sigma}$,

$$\begin{aligned}
\mathbf{m}(\mathbf{y}_j;\mathbf{H}) &= \mathbf{H}\frac{\nabla F(\mathbf{y}_j;\mathbf{H})}{F(\mathbf{y}_j;\mathbf{H})} \\
&\simeq \mathbf{H}\frac{\alpha\Phi(\mathbf{y}_j;\mathbf{u},\mathbf{\Sigma}+\mathbf{H})(\mathbf{\Sigma}+\mathbf{H})^{-1}(\mathbf{u}-\mathbf{y}_j)}{\alpha\Phi(\mathbf{y}_j;\mathbf{u},\mathbf{\Sigma}+\mathbf{H})} \\
&= \mathbf{H}(\mathbf{\Sigma}+\mathbf{H})^{-1}(\mathbf{u}-\mathbf{y}_j). \qquad (7)
\end{aligned}$$

Further rewriting Eq.(7) results in a linear matrix equation of unknown $\mathbf{\Sigma}$,

$$\mathbf{\Sigma}\mathbf{H}^{-1}\mathbf{m}_j = \mathbf{b}_j \qquad (8)$$

where $\mathbf{m}_j \equiv \mathbf{m}(\mathbf{y}_j;\mathbf{H})$ and $\mathbf{b}_j \equiv \mathbf{u}-\mathbf{y}_j-\mathbf{m}_j$.

An over-complete set of the linear equations can be formed by using all the trajectory points $\{\mathbf{y}_j | j = 1,..,t_u\}$ located within the basin of attraction $\mathcal{S}$. For efficiently collecting a sufficient number of samples $\{(\mathbf{y}_j,\mathbf{m}_j)\}$, we run N_2 mean shift procedures initialized by sampling the neighborhood of $\mathbf{u}$ uniformly. This results in t_u samples ($t_u = \sum_{i=1}^{N_2} t_i$), where t_i denotes the number of points on the convergent trajectory

starting from $\mathbf{x}_i$. The system described in Eq.(8) is solved by considering the following constrained least-squares problem [34, 35],

$$\begin{array}{rcl} \mathbf{A}\boldsymbol{\Sigma} & = & \mathbf{B} \\ \boldsymbol{\Sigma} & \in & \mathcal{SPD} \\ \mathbf{A} & = & (\mathbf{m}_1, .., \mathbf{m}_{t_u})^t \mathbf{H}^{-t} \\ \mathbf{B} & = & (\mathbf{b}_1, .., \mathbf{b}_{t_u})^t \end{array} \tag{9}$$

where $\mathcal{SPD}$ denotes a set of symmetric positive definite matrices in $\mathcal{R}^{d \times d}$.

Following [36], the unique solution $\boldsymbol{\Sigma}^{**}$ of Eq.(9) is expressed by,

$$\boldsymbol{\Sigma}^{**} = \mathbf{U}_P \boldsymbol{\Sigma}_P^{-1} \mathbf{U}_{\tilde{Q}} \boldsymbol{\Sigma}_{\tilde{Q}} \mathbf{U}_{\tilde{Q}}^t \boldsymbol{\Sigma}_P^{-1} \mathbf{U}_P^t \tag{10}$$

which involves symmetric Schur decompositions [35, p.393] of the matrices $\mathbf{P} \equiv \mathbf{A}^t\mathbf{A}$ and $\tilde{\mathbf{Q}} \equiv \boldsymbol{\Sigma}_P \mathbf{U}_P^t \mathbf{Q} \mathbf{U}_P \boldsymbol{\Sigma}_P$ given $\mathbf{Q} \equiv \mathbf{B}^t\mathbf{B}$, i.e.,

$$\begin{array}{rcl} \mathbf{P} & = & \mathbf{U}_P \boldsymbol{\Sigma}_P^2 \mathbf{U}_P^t \\ \tilde{\mathbf{Q}} & = & \mathbf{U}_{\tilde{Q}} \boldsymbol{\Sigma}_{\tilde{Q}}^2 \mathbf{U}_{\tilde{Q}}^t. \end{array}$$

The solution $\boldsymbol{\Sigma}^{**}$ is derived from finding $\mathbf{Y}^{**}$ in the Cholesky factorization of $\boldsymbol{\Sigma} = \mathbf{Y}\mathbf{Y}^t$. It can be shown that $\boldsymbol{\Sigma}^{**}$ uniquely minimizes an area criterion $\|\mathbf{A}\mathbf{Y} - \mathbf{B}\mathbf{Y}^{-t}\|_F^2$ where $\|.\|_F$ denotes the Frobenius norm. This area criterion is related to the total least-squares [37] since errors in both $\mathbf{A}$ and $\mathbf{B}$ are considered for the minimization.

2.6 Scale Selection Criterion

The multi-scale analysis treats $\mathbf{H}$ as a variable parameter. It is supposed that a set of analysis bandwidths $\{\mathbf{H}_k | k = 1, .., K\}$ is given *a priori*. Our scale selection criterion is based on the stability test [33]. Given a set of estimates $\{(\mathbf{u}_k, \boldsymbol{\Sigma}_k)\}$ for a series of the successive analysis bandwidths, a form of the Jensen-Shannon divergence is defined by,

$$JS(k) = \frac{1}{2} \log \frac{|\frac{1}{2a+1} \sum_{i=k-a}^{k+a} \boldsymbol{\Sigma}_i|}{\sqrt[2a+1]{\prod_{i=k-a}^{k+a} |\boldsymbol{\Sigma}_i|}} + \frac{1}{2} \sum_{i=k-a}^{k+a} (\mathbf{u}_i - \mathbf{u})^t (\sum_{i=k-a}^{k+a} \boldsymbol{\Sigma}_i)^{-1} (\mathbf{u}_i - \mathbf{u}) \tag{11}$$

where $\mathbf{u} = \frac{1}{2a+1} \sum_{k-a}^{k+a} \mathbf{u}_i$ and a define the neighborhood width of the divergence computation. The most stable estimate across the analysis bandwidths provides a local minimum of the divergence profile. We treat this result as the final estimation of our multi-scale analysis $(\mathbf{u}^*, \boldsymbol{\Sigma}^*)$.

3 Statistical Verification

In this section, we present a goodness-of-fit measure for validating the resulting estimates. Such statistical verification gives a principled means for rejecting accidental ill-estimates. We treat this problem as analysis of chi-square fitting residual errors. We employ a linear model with an additive parameter of the DC component; $f \simeq \alpha \times \Phi + \beta$. Recall that our estimation model in Eq.(1) is without the DC. The additional degree of freedom introduced serves as another goodness-of-fit indicator. Given the estimate pair ($\mathbf{u}^*$,$\mathbf{\Sigma}^*$), the following defines the signal response estimate $\hat{f}$ with two unknowns,

$$\hat{f}(\mathbf{x}, \mathbf{u}^*, \mathbf{\Sigma}^*; \alpha, \beta) = \alpha \times [\Phi(\mathbf{x}; \mathbf{u}^*, \mathbf{\Sigma}^*)]_{\mathbf{x} \in \mathcal{S}} + \beta. \tag{12}$$

where $\mathcal{S}$ is a set of data points in the neighborhood of $\mathbf{u}$, belonging to the basin of attraction of $\mathbf{u}$, as introduced in Eq.(1). The chi-square statistic indicates the residual error of the fitted model $\hat{f}(\mathbf{x})$ [38, p.660],

$$\chi^2 \equiv \sum_{\mathbf{x}_i \in \mathcal{S}'} (\frac{f(\mathbf{x}_i) - \hat{f}(\mathbf{x}_i)}{\sigma_i})^2 = \sum_{\mathbf{x}_i \in \mathcal{S}'} (\frac{f(\mathbf{x}_i) - \alpha\Phi(\mathbf{x}_i) - \beta}{\sigma_i})^2 \tag{13}$$

where σ_i is local uncertainty of normally distributed error $(f(\mathbf{x}_i) - \hat{f}(\mathbf{x}_i))^2$ and $\mathcal{S}'$ denotes an appropriate support of the data space, within which the verification process performs sampling. Note that this verification support $\mathcal{S}'$ may be different from the model support $\mathcal{S}$, which will be discussed in Section 6.2 [p.19].

Parameters α and β are estimated by chi-square fitting. Since both are non-negative, we introduce parameters a and b such that $\alpha = a^2$ and $\beta = b^2$. The estimates α^* and β^* are given by solving $\partial\chi^2/\partial a = 0$ and $\partial\chi^2/\partial b = 0$,

$$(\alpha^*, \beta^*) = \begin{cases} (p, q) & \text{if p} > 0 \text{ and q} > 0 \\ (\frac{\sum f(\mathbf{x}_i)\Phi(\mathbf{x}_i)}{\sum \Phi(\mathbf{x}_i)^2}, 0) & \text{if p} > 0 \text{ and q} \leq 0 \\ (0, \frac{\sum f(\mathbf{x}_i)}{N_s}) & \text{if p} \leq 0 \text{ and q} > 0 \\ (0, 0) & \text{if p} \leq 0 \text{ and q} \leq 0 \end{cases} \tag{14}$$

where $\sigma = \sigma_i$ for all i,

$$p = \frac{N_s \sum f(\mathbf{x}_i)\Phi(\mathbf{x}_i) - \sum f(\mathbf{x}_i) \sum \Phi(\mathbf{x}_i)}{N_s \sum \Phi(\mathbf{x}_i)^2 - (\sum \Phi(\mathbf{x}_i))^2} \tag{15}$$

$$q = \frac{\sum f(\mathbf{x}_i) \sum \Phi(\mathbf{x}_i)^2 - \sum \Phi(\mathbf{x}_i) \sum f(\mathbf{x}_i)\Phi(\mathbf{x}_i)}{N_s \sum \Phi(\mathbf{x}_i)^2 - (\sum \Phi(\mathbf{x}_i))^2} \tag{16}$$

and N_s is the number of samples in $\mathcal{S}'$ and all the summations are over $\mathbf{x}_i \in \mathcal{S}'$.

Given the above parameter estimates, χ^2 is computed by using Eq.(13). Chi-square probability function Q [38, p.221] is employed to indicate an ill-fit of our model to the given signal,

$$Q(\chi^2|\nu) = Q(\frac{N_s - M}{2}, \frac{\chi^2}{2}) = g(\frac{N_s - M}{2}, \frac{\chi^2}{2}). \tag{17}$$

In Eq.(17), g is the incomplete gamma function [38, ch.6.2] with the number of degrees of freedom $\nu = (N - M)/2$, and M is the number of parameters.

Finally, we obtain the following rejection criterion,

$$\text{Reject } (\mathbf{u}^*, \mathbf{\Sigma}^*) \text{ if } Q < th_1 \text{ or } \beta^* > th_2. \tag{18}$$

The threshold for Q is set conservatively to the common confidence level $th_1 = 0.001$ [38, p.664]. Having a large estimate for β also indicates an ill-fit with our estimation model without the DC. The threshold th_2 for β can be learned from training samples for specific applications.

4 Volumetric Measurements

This section presents our solutions for deriving volumetric measurements of the target tumor from the Gaussian model fitted to the data. First, tumor boundary segmentation is approximated by a 3D ellipsoid defined from the fitted model. We propose solutions for analytically deriving target tumor's i) volume, ii) maximum diameter, and iii) average diameter, and iv) isotropy, directly from the ellipsoidal segmentation result. An extension of these solutions towards arbitrary voxel dimensions will also be provided.

The multi-scale Gaussian-based model fitting, described in Section 2, results in the mean and covariance estimates $(\mathbf{u}^*, \mathbf{\Sigma}^*)$ of a Gaussian function that fits the given data best. Treating the fitted model as a normal probability distribution $\mathcal{N}(\mathbf{x}; \mathbf{u}^*, \mathbf{\Sigma}^*)$, the tumor boundary segmentation can be approximated by a confidence ellipsoid forming a 3D equal-probability contour. Such a confidence ellipsoid is defined by the following generic quadratic equation,

$$(\mathbf{x} - \mathbf{u}^*)^t \mathbf{\Sigma}^{*-1} (\mathbf{x} - \mathbf{u}^*) = \sigma^2 \tag{19}$$

where σ^2 is a squared Mahalanobis distance, defining the confidence limit. A specific value of the confidence limit σ^2 has to be chosen so that the equal-probability contour coincides well with the tumor boundary. Throughout this paper, we use an empirically determined value $\sigma^2 = 1.6416$, corresponding to the 35% confidence limit. Fig.3 and Fig.4 illustrate the segmentation results with this confidence limit.

Given σ^2, the volumetry of an ellipsoid can be determined as a function of three radii along its major and two minor orthogonal axes. The radii are denoted by $r_i > 0$ $(r_1 \geq r_2 \geq r_3)$. The following derives r_i from the eigen decomposition of the covariance $\mathbf{\Sigma}^*$. Such eigen decomposition can be expressed in a matrix equation: $\mathbf{\Sigma}^*\mathbf{V} = \mathbf{V}\mathbf{\Lambda}$. $\mathbf{V}$ is a column matrix of the eigenvectors $\mathbf{v}_i$ and $\mathbf{\Lambda}$ is a diagonal matrix of the corresponding eigenvalues λ_i^2 $(\lambda_1 \geq \lambda_2 \geq \lambda_3)$. Right-multiply the matrix equation with $\mathbf{V}^t$ yields the symmetric Schur decomposition of $\mathbf{\Sigma}^*$: $\mathbf{\Sigma}^* = \mathbf{V}\mathbf{\Lambda}\mathbf{V}^t$. Since $\mathbf{\Sigma}^{*-1} = \mathbf{V}\mathbf{\Lambda}^{-1}\mathbf{V}^t$, with a coordinate transform $\mathbf{y} \equiv \mathbf{V}^t(\mathbf{x} - \mathbf{u}^*)$, Eq.(19) can be simplified to: $\mathbf{y}^t\mathbf{\Lambda}^{-1}\mathbf{y} = \sigma^2$. Substituting three points, $\mathbf{y} = (r_1, 0, 0)^t, (0, r_2, 0)^t, (0, 0, r_3)^t$, which are known to lie on the ellipsoid surface, to the quadratic equation results in,

$$r_i = \sigma\lambda_i \tag{20}$$

As a result, the following volumetric measurement formulae can immediately be derived for the volume $V = \frac{4}{3}\pi\sigma^3\prod_i \lambda_i$, the maximum diameter $L = 2\sigma\lambda_1$, the average diameter $A = \frac{2}{3}\sigma\sum_i \lambda_i$, and the isotropy $R = \frac{\lambda_2+\lambda_3}{2\lambda_1}$, where V, L, and A are in the voxel unit and the isotropy R ranges in $[0, 1]$, taking the value 1 when it becomes a sphere. The bias of these volumetric measurements are caused solely by the segmentation error. Therefore, these formulae are exact thus free from the partial volume effect when the tumor boundary is well-characterized by the ellipsoidal segmentation.

Given a voxel dimension in a physical unit, the volumetric measurement formulae above can be revised to produce the measurements in the unit. This is a crucial step for any comparative and differential studies because the voxel dimension can vary across different scans. Suppose that a voxel dimension is given as $(\Delta x, \Delta y, \Delta z)$ in millimeter or any other unit. After a coordinate transform, eigenvalues in the unit of millimeter, λ_i', can be expressed as a function of the voxel dimensions and eigenvectors,

$$\lambda_i' = \beta_i\lambda_i \tag{21}$$

$$\beta_i = \sqrt{(v_{xi}\Delta x)^2 + (v_{yi}\Delta y)^2 + (v_{zi}\Delta z)^2} \tag{22}$$

where the eigenvector is denoted by $\mathbf{v}_i = (v_{xi}, v_{yi}, v_{zi})^t$. This leads us to the following formulae which

takes the voxel dimension into account,

$$V' = \frac{4}{3}\pi\sigma^3 \prod_i \beta_i\lambda_i \quad (23)$$

$$L' = 2\sigma\lambda'_1 = 2\sigma \max_i \beta_i\lambda_i \quad (24)$$

$$A' = \frac{2}{3}\sigma \sum_i \beta_i\lambda_i \quad (25)$$

$$R' = \frac{\lambda'_2 + \lambda'_3}{2\lambda'_1} \quad (26)$$

where $\lambda'_1 \geq \lambda'_2 \geq \lambda'_3$. Note that λ'_i must be re-sorted from the original order given by the eigen decomposition because the coordinate transform may change such an order.

5 Algorithm Overview

The proposed algorithm consists of three stages: i) the anisotropic structure estimation ii) the verification of the estimates, and iii) volumetric measurements. The first stage assumes that a marker indicating the rough location of the target nodule is given *a priori*. Such information can be provided by a user of a GUI-based system (see Section 6.3 for example). The estimation algorithm is presented below.

Problem Given the 3D input data $f(\mathbf{x})$, a marker point $\mathbf{x}_p$, a set of analysis scales $\{\mathbf{H}_k | k = 1, ..., K\}$, estimate the 3D anisotropic structure of a nodule ($\mathbf{u}^*$, $\mathbf{\Sigma}^*$).

Scale-specific estimation For each k,

1. Perform uniform sampling centered at x_p, resulting in a set of N_1 starting points.
2. Perform the mean shift procedure in Eq.(6) from each starting point.
3. Take the convergence point of the majority of the points as the location estimate $\mathbf{u}_k$.
4. Perform uniform sampling centered at $\mathbf{u}_k$, resulting in a set of N_2 starting points.
5. Perform the mean shift procedure from each starting point.
6. Construct the system in Eq.(9) with the mean shift vectors $\{\mathbf{m}(\mathbf{y}_j)\}$ along the converging trajectories.
7. Solve the system by Eq.(10), resulting in the covariance estimate $\mathbf{\Sigma}_k$.

Scale selection With K estimates $\{(\mathbf{u}_k, \mathbf{\Sigma}_k)\}$,

1. Compute the divergence $\{JS(\mathbf{u}_k, \mathbf{\Sigma}_k)\}$ using Eq.(11) for $k = 1 + a, ..., K - a$.
2. Find the most stable solution $(\mathbf{u}^*, \mathbf{\Sigma}^*)$ by finding a local minimum of $\{JS_k\}$: $argmin_k JS(\mathbf{u}_k, \mathbf{\Sigma}_k)$.

The second stage provides the binary decision of acceptance or rejection of the estimates in the following algorithm.

Problem Given the 3D input data $f(\mathbf{x})$ and thresholds th_1 and th_2, verify the estimate ($\mathbf{u}^*$, $\mathbf{\Sigma}^*$) for the acceptance or rejection decision.

Statistical verification With ($\mathbf{u}^*$, $\mathbf{\Sigma}^*$),

1. Compute α^* and β^* by the chi-square fitting of Eq.(14).
2. Compute χ^2 by Eq.(13).
3. Compute the Chi-square probability $Q(\chi^2)$ by Eq.(17).
4. Apply Eq.(18) to Q and β^*. Reject ($\mathbf{u}^*$, $\mathbf{\Sigma}^*$) if Eq.(18) holds otherwise accept it.

The ellipsoidal segmentation of the accepted nodule estimate is given by the 35% confidence ellipsoid of the normal distribution $N(\mathbf{u}^*, \mathbf{\Sigma}^*)$ in the form of Eq.(19) with $\sigma^2 = 1.6416$. The third stage provides a number of volumetric measurements of the accepted estimate,

Problem Given the accepted estimate ($\mathbf{u}^*$, $\mathbf{\Sigma}^*$) and the voxel dimension $(\Delta x, \Delta y, \Delta z)$, provide the volumetric measurements of the target nodule.

Volumetric Measurements With ($\mathbf{u}^*$, $\mathbf{\Sigma}^*$), σ^2, and $i \in (1, 2, 3)$,

1. Compute the eigen decomposition $(\mathbf{v}_i, \lambda_i)$ of $\mathbf{\Sigma}^*$.
2. Compute β_i by Eq.(22).
3. Sort the transformed eigenvalues λ_i' in Eq.(21).
4. Derive the tumor volume V' by Eq.(23).
5. Derive the maximum diameter L' of the tumor by Eq.(24).
6. Derive the average diameter A' of the tumor by Eq.(25).
7. Derive the tumor isotropy R' by Eq.(26).

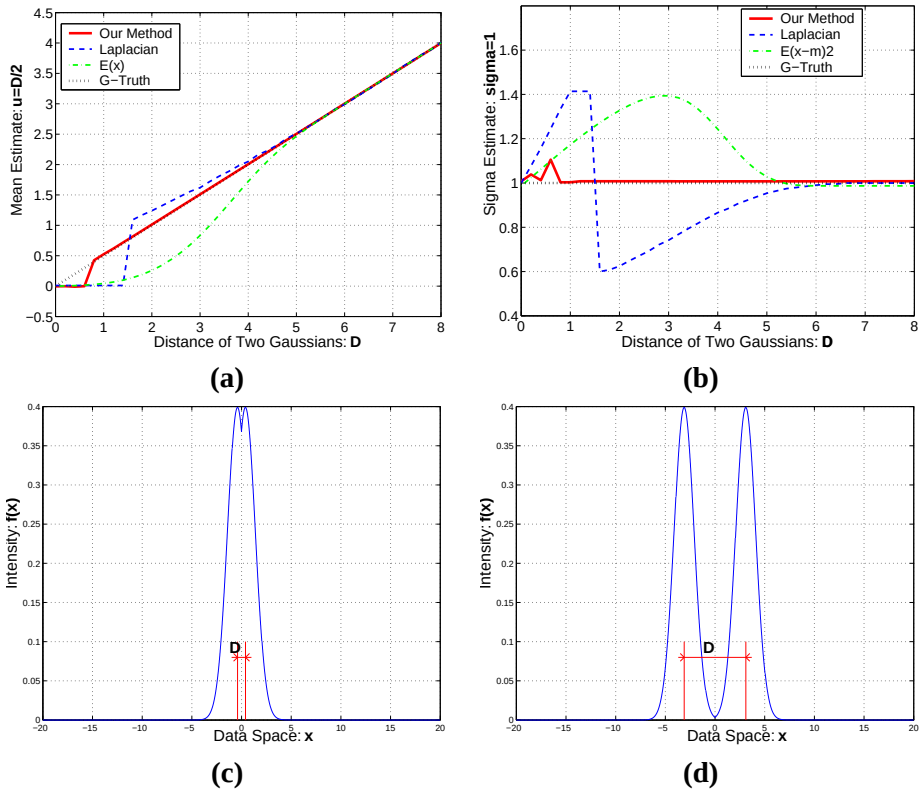

Figure 2: Comparison of our method (solid-line) with γ-normalized Laplacian (dashed-line) and standard sample estimate (dot-dashed-line) using 1D synthetic data. The ground-truth $\mathbf{u} = D/2$ and $\mathbf{\Sigma} = \sigma = 1$ are denoted by dotted-line. Test data is generated by superimposing two Gaussians with a varying distance D for evaluating robustness of estimates against biases caused by neighboring structures. (a): local maxima estimates, (b): scale estimates, (c): our method's break-point $D = 0.8$, below which estimations are subjected to the bias. (c): γ-normalized Laplacian's break-point $D = 6.2$.

6 Experimental Results

6.1 Synthetic Data

The proposed framework is examined with 1D and 2D synthetic data with the presence of noise. Fig.2 compares local maximum and scale estimates by a 1D implementation of our algorithm with those by the γ-normalized Laplacian [1] and the standard sample estimation [2, p.179]. The test data is generated at each location by taking the maximum of two superimposed 1D Gaussians offset by a varying distance D between the two peaks. The one in right is treated as the target while the left one acts as a non-target neighboring structure. Each Gaussian has the same variance $\mathbf{\Sigma} = 1$ and hight $\alpha = 1$. Fig.2(a,b) show the estimated mean and variance of the target as a function of the varying distance D. The ground-truth mean and variance are $(\mathbf{u} = D/2, \mathbf{\Sigma} = \sigma = 1)$. Fig.2(c,d) show the break-points by our and γ-normalized Laplacian methods,

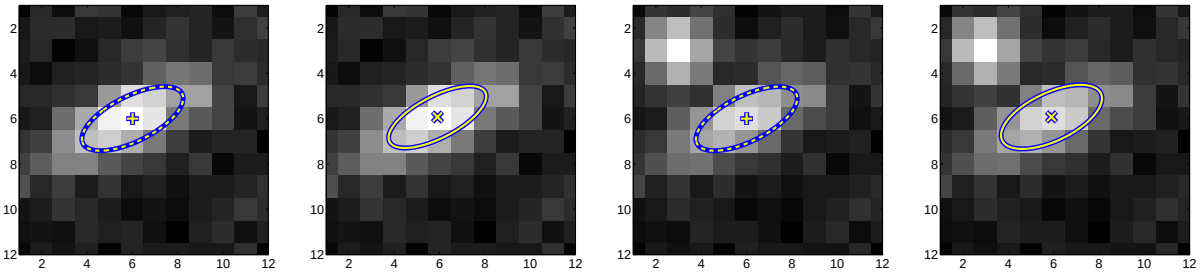

(a) **(b)** **(c)** **(d)**

Figure 3: Examples with 2D synthetic data. (a) and (b) illustrate the ground-truth and our method's estimate for an anisotropic Gaussian $\mathbf{\Sigma}$=[2 -2;-2 5] with random additive noise. (c) and (d) show those for two Gaussians with the noise. The center of the smaller Gaussian is deviated by 2 Mahalanobis distance away from the target Gaussian. "+" and dashed-ellipses indicate ground-truth local maximum and spread. "x" and solid-ellipses display those estimated by our 2D algorithm.

respectively. The break-point is defined as the distance of the two peaks, below which estimations are subjected to the bias due to the margin-truncation effect described in the introduction. The 1D system employs all the available data points ($N_1 = N_2 = N_S$) and 40 analysis scales with 0.05 interval ($h = (0.1^2, 0.15^2, .., 2^2)$ for $\mathbf{H} = h\mathbf{I}$). For the sample variance estimation, the densities $p(x_i)$ are approximated by $f(x_i)$ normalized by the probability mass within $\pm 1\sigma$ around the true maximum. The results indicate much lower break-point of our method than of others. This suggests that our method can achieve robust and accurate estimations even with the presence of the severe margin-truncations, demonstrating the advantage of our framework. Fig.3 shows examples with 2D synthetic data. A 2D implementation of our method are applied for two test data: i) the 2D target Gaussian with random noise (3(a)) and ii) the same target with the same noise and a non-target Gaussian (3(c)). The ground-truth and their corresponding estimates by our method are shown as 35% confidence ellipses in Fig.3(a,c) and Fig.3(b,d), respectively. This 2D implementation utilizes all available data points and 12 analysis scales ($h = (0.5^2, 0.75^2, .., 3.25^2)$). The results are almost identical to the ground-truth despite the presence of the random noise and the neighboring structure, confirming the results of our 1D experiment.

6.2 Lung HRCT Data

A 3D implementation of the proposed algorithm is evaluated with two clinical data sets of the thin-section (1.25 mm slice thickness) chest high-resolution computed tomography (HRCT) images including pathological lesions. The data is recorded by Multislice CT scanners (Somatom Volume Zoom and Somatom Sensation 16; Siemens) and anonymatized. Each volumetric image consists of 12-bit positive values over an

array of 512x512 lattices. The number of slices in a CT volume and the dimensions of a voxel vary across volumes in our data set. The number of slices ranges between 217 and 616. The voxel dimensions range within $[0.4609 - 0.8281, 0.4609 - 0.8281, 0.5 - 1]$ in millimeter.

A straightforward implementation of our algorithm without any 3D specific adaptation provides the 3D nodule analysis system. The marker locations are provided by trained radiologists. Our visual inspection with a 3D renderer revealed however that most of the markers are noticeably off-centered, deviating from the (unknown) true nodule centers with a certain degree. A 33-voxel cubic volume-of-interest (VOI) is extracted for processing each nodule. The analysis bandwidths are given by 18 scales with 0.25 interval $h = (0.50^2, 0.75^2, .., 4.75^2)$. Uniform sampling in the 3-voxel neighborhood of the marker (i.e., $N_1 = 7$) is used for estimating local maximum. The 3-voxel size is determined empirically. The same strategy is employed for initializing the mean shift trajectories around the local maximum (i.e., $N_2 = 7$). The neighborhood width of the divergence computation is set to $a = 1$ (considering only three adjacent scales). For the verification, all data points that lie within the 90% confidence ellipsoid of $(\mathbf{u}^*, \mathbf{\Sigma}^*)$ are used as the support $\mathcal{S}'$. This includes data points that may not converge to the estimated nodule center. For parameter estimation, it is natural to exclude such samples in order to realize a robust algorithm. For verification, however, such non-convergence of samples also provide valid information of the model being ill-fit thus should be kept for improving the rejection-acceptance margin. The rest of parameters are set as follows. The degrees of freedom in Eq.(17) are given by $M = 3 + 6 + 2 = 11$. The β threshold in Criterion(18) is set to $th_2 = 400$. The global uncertainty σ in Eq.(13) is estimated from the sample variance of 77 lesions, resulting in $\sigma = 356$.

The first data set consists of HRCT images of 14 patients including the total of 77 pulmonary nodules. All of the nodules are small ($<$10mm). The data is recorded by a Siemens Somatom volume zoom scanner. Due to the lack of ground-truth for nodule center and segmentation, the classification of the correct or failure estimation is given manually by eye-appraisal of experts using a 3D render view and its corresponding 3 orthogonal slice views (Fig.6 shows an example of such views). The results of performance evaluations with this data set are given as follows. 63 cases (81.8%), including all the solitarty nodules, resulted in correct estimation. All the 14 failures were successfully rejected by the verification process without false rejection and false acceptance. Most of the failures were due to very small nodules ($<$5mm) that are heavily embedded into pleural surface. Given an off-centered marker, this can cause a nearby rib to be falsely estimated as nodule center (e.g., Fig.5). The data includes six cases of the part- and non-solid or ground-glass opacity nodules classified by the radiologists (GGO nodules, see Fig.1c,d and Fig.4a,b). All the GGO

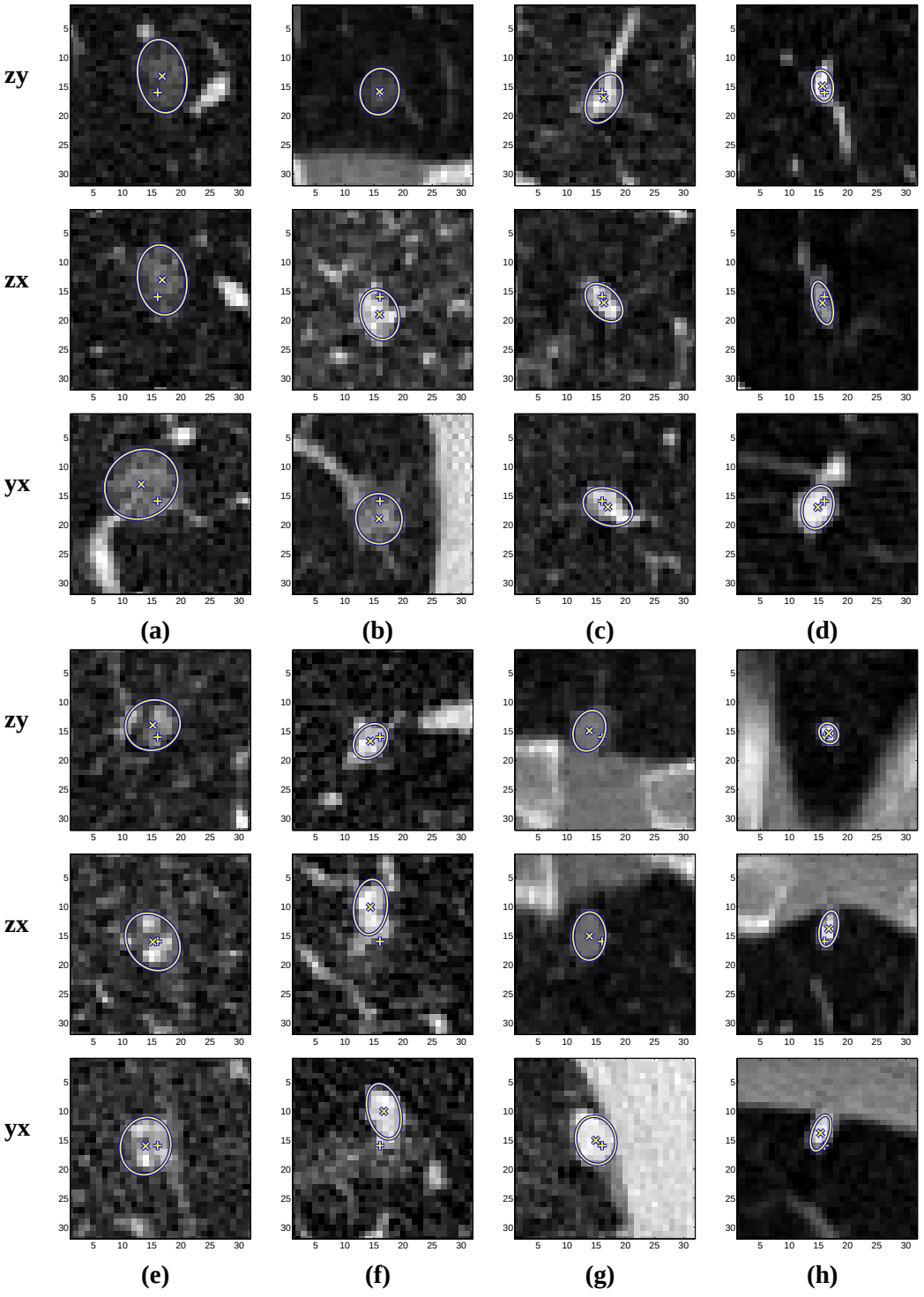

Figure 4: Examples of the estimation results with 3D HRCT data. The marker locations are indicated by "+". The estimated local maxima are indicated by "x". The estimated spread of the nodules are shown as 2D intersections of 35% confidence ellipsoids. Cases (a) and (b) are non-solid (GGO) nodules identified by experts. Cases (c) to (f) are vascularized nodules with irregular non-spherical shapes. Cases (g) and (h) illustrate nodules attached to pleural surface.

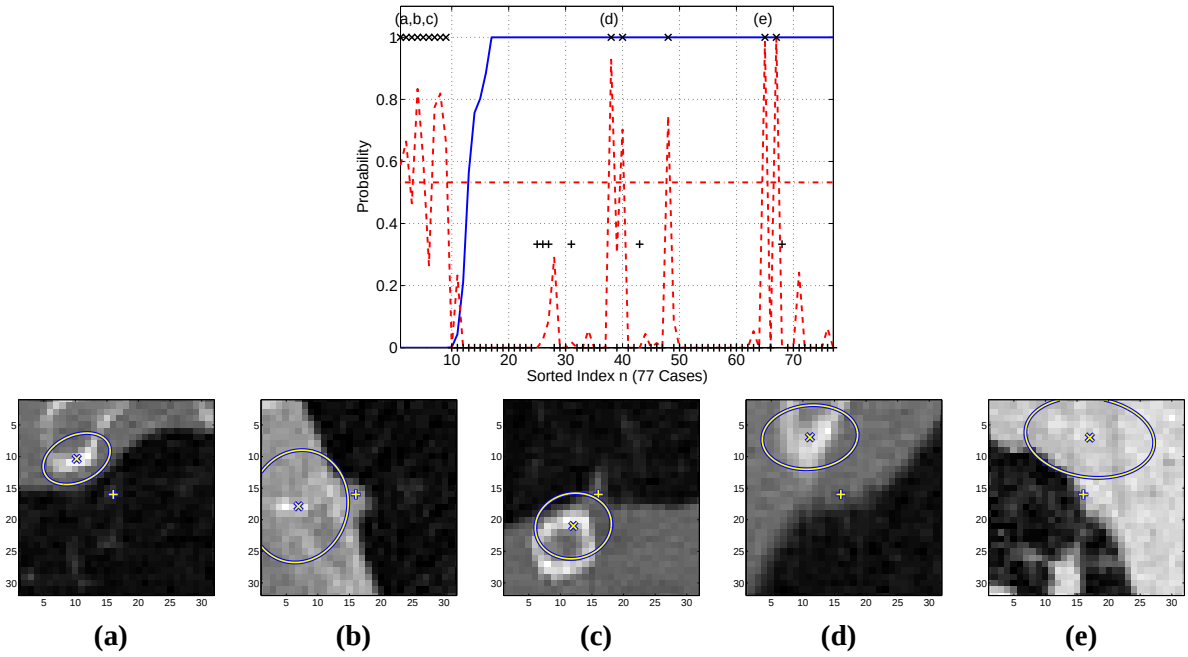

Figure 5: Experimental results for the verification process. The top plot illustrates the Q probability (solid-line) and β estimate (dashed-line) for each test case. The symbols "+" and "x" indicate correct and failure cases, respectively. The correct symbol "+" placed above zero also indicate non-solid (GGO) nodule cases. β values are normalized to fit within the range of this plot. A horizontal dashed-line indicates the β-threshold $th_2 = 400$. The bottom images show examples of correctly rejected failures. Legend of these images are the same as Fig.4. Cases (a) and (c) satisfied the rejection conditions of both Q and β while Case (b) met only the Q condition and Cases (d) and (e) met only the β condition.

nodules were successfully estimated and accepted.

Fig.4 shows examples of the resulting center and spread estimates. It illustrates cases with the irregular, non-solid (GGO), and juxtapleural nodules whose geometrical shapes and/or intensity distributions are largely deviated from the Gaussian structure. The correct estimations for these difficult cases demonstrate the robustness and effectiveness of our framework. Fig.5 shows the results of the statistical verification and examples of the rejected cases. For evaluating the generalization capability, we apply the same verification process to the data of 3 patients who are different from the ones used for deriving the parameters σ and th_2. This experiment resulted in 96% correct verification rate (4 false acceptances among 100 trials), similar to the results shown in Fig.5.

The second data set is much larger than the first set, consisting of HRCT images of 39 patients with the total of 1310 pulmonary nodules. Moreover, the data is recorded by multiple scanners (Somatom volume zoom and Somatom Sensation 16; Siemens), and the data includes much wider range of nodule sizes (3-30

Estimation	# Cases (%)	Verification	# Cases (%)
Correct	1064 (81.2)	**TP**	995 (76.0)
		FN	69 (5.2)
Failure	246 (18.8)	**TN**	205 (15.7)
		FP	41 (3.1)

Table 1: Results of performance evaluation of our method with the large data set. The data set consists of 39 patients with 1310 nodules whose size ranges from 3 mm to 30 mm. Multiple scanners are used for data collection. TP: true positive, accepted correct estimates. FN: false negative, rejected correct estimates. TN: true negative, rejected false estimates. FP: false positive, accepted false estimates.

mm). Thus evaluation with this data set provides more realistic performance benchmark of our method in the clinical settings. The same system, including the parameter values for both estimation and verification, is used for this evaluation.

Table 1 summarized the results. 1064 cases (81.2%) resulted in successful estimation confirmed by the same visual inspection used for the small data set. This correct estimation rate was almost identical to the one for the first smaller data set, confirming the scalability of our algorithm. Similar to the first data set, most failures were caused by small juxtapleural nodules. Note that our method resulted in correct estimation for many juxtapleural cases as shown in Fig.4g-h. When a juxtapleural nodule is very small and deeply embedded into the surface, however, our method tends to provide biased estimates since the tumor center may not correspond to spatial maximum for such cases. For verification, small percentage of cases resulted in false acceptance (false positive (FP): 3%) and false rejection (false negative (FN): 5%), similar to the results of the generalization experiment with 100 trials. The most false positive cases occurred when a marker was placed outside of the attraction basin of the target nodule, causing the characterization of a nearby non-pathological structure (e.g., rib bones and vessels) which was accidentally Gaussian-like. On the other hand, the false negative cases were mostly caused by heavily vascularized or wall-embedded nodules that were correctly characterized by our robust algorithm but classified as non-nodule due to large chi-square fitting error. Except for these special cases, the majority of both correct and incorrect estimates are successfully accepted and rejected, respectively.

Another important question is the *stability* or *robustness* of our system against the initial localization of the markers. Such stability is a key factor for realizing low intra- and inter-operator variability and high reproducibility. First, we study the characterization performance with additional duplicate markers. The second data set contained 150 additional duplicate markers provided by the radiologists, which are deviated from the other indicating the same nodule within 6 Euclidean voxel distance. Including these markers, the

Range	σ**Mean**	σ**Cov**	σ**Vol**	σ**MaxD**	σ**AveD**	σ**Iso**
$\sqrt{\mathbf{1}}$	0.49	2.78	52.9	0.41	0.22	0.014
$\sqrt{\mathbf{2}}$	0.58	2.49	44.1	0.46	0.28	0.018
$\sqrt{\mathbf{3}}$	0.56	2.51	45.4	0.45	0.27	0.017

Table 2: The standard deviation of the various estimates induced by random perturbation of initial marker locations within three sampling ranges, $\sqrt{1}$,$\sqrt{2}$, and $\sqrt{3}$ Mahalanobis distance, around the tumor center estimated from the marker given by the radiologists. σMean: the average of standard deviations (SD) for single coordinate variables, σCov: SD of the Frobenius matrix norm, σVol: SD of the 3D volume in $voxel^3$ unit, σMaxD: SD of the maximum diameter in $voxel$ unit, σAveD: SD of the average diameter in $voxel$ unit, and σIso: SD of the isotropy parameter ranging within [0,1].

Range (Vol,AveD)	**<(150,6.7)**	**<(525,10)**	**<(1250,13.3)**	**<(2425.16.7)**	**<(4190,20)**
σ**Vol**	4.00	15.9	21.0	39.6	45.4
σ**AveD**	0.13	0.25	0.25	0.27	0.27
σ**MaxD**	0.23	0.42	0.42	0.44	0.45

Table 3: The standard deviation of the volumetric estimates shown as a function of five different tumor size ranges. The ranges are described in both volume (Vol) and average diameter (AveD) in $voxel^3$ and $voxel$ units, respectively. The largest sampling range, $\sqrt{3}$, is used for this experiment.

same performance evaluation for Table 1 is carried out with the total of 1469 markers. The results were almost identical to the ones without the duplicate markers; correct estimation: 81.3%, failed estimation: 18.7%, true positive: 76.3%, false negative: 5.0%, true negative: 15.4%, false positive: 3.3%.

Second, the robustness is evaluated by numerical stability analysis of estimation variances induced by random perturbation of initial marker locations. For this experiment, we randomly select 550 nodules from the second database which are correctly estimated and verified (confirmed by our eye appraisal) and are of size between 3 and 20 voxels in the average diameter. For each selected nodule, its mean and covariance are estimated by our method from the marker given by the radiologists. A set of 10 test markers are randomly sampled around the estimated mean within $\sqrt{3}$ Mahalanobis distance range for each nodule. The variance of estimates with the 5500 test markers are studied for center (mean), spread (covariance), volume, maximum/average diameter, and isotropy.

Table 2 and 3 summarize the results shown as a function of sampling ranges and tumor sizes, respectively. The spread variance σCov is quantified by the standard deviation of the Frobenius norm of the covariance matrix. While the isotropy parameter is non-dimensional, the variance for the center, volume, maximum/average diameters are expressed by the standard deviation of the estimates in $voxel$ unit. Since the voxel dimension of our data is bounded by a 1 mm cube and roughly isotropic, these volumetric estimate variances in $voxel$ unit can be treated as an upper-bound of the variances in *millimeter* unit for the

measurements by using Eq.(23-26). The results in Table 2 show that the various estimation variances do not change largely by using the different sampling ranges from $\sqrt{1}$ to $\sqrt{3}$ Mahalanobis distances, indicating the insensitivity against the marker perturbation. The absolute values for the mean location and spread variances are also very small, showing the robustness of our estimation process. Table 3 shows that the absolute value of the estimation variances correlates better to the estimated tumor sizes. For the given range of the tumor sizes, the standard deviations with the $\sqrt{3}$ Mahalanobis distance perturbation were small with respect to the corresponding tumor sizes, ranging between 1-3% of the estimated measurement values. The overall results of the above stability analyses suggest the insensitivity of our solution against the initialization or intra- and inter-operator variability. Due to the lack of the ground-truth, the error analysis of the estimation bias was not possible. However the eye appraisal of the results using the visualization in the form of Fig.4 and 6 indicated at least reasonable accuracy of the mean location and maximum diameter estimates.

6.3 System Implementation

The above-described 3D nodule analysis system is implemented in C language and processes each 33-voxel volume-of-interest (VOI) by an average of two seconds using an off-the-shelf PC with a 2.4GHz Intel CPU. A quasi real-time nodule characterization and visualization software is developed by using this system. The C-implemented system is packaged as the matlab's mex library which is used as a computational module of a volume visualization tool built on the matlab's GUIDE (GUI development environment). Fig.6 illustrates screen-snapshots of the nodule characterization and visualization process.

7 Discussions

This article proposed a comprehensive robust framework for characterizing the 3D anisotropic pulmonary nodules. The nodule's geometric structure is specified by a 3D ellipsoid that is provided by robustly fitting the anisotropic Gaussian-based intensity model to the volume data. The new estimation framework unifies the mean shift-based robust statistical analysis and the linear scale-space-based multi-scale analysis. The unification is realized by formally extending the density mean shift towards the continuous positive function representing the volume data. The proposed verification algorithm also complements the estimation framework, providing an effective goodness-of-fit measure for rejecting accidental ill-estimates. The analytical volumetric measurement solutions are also proposed for efficiently approximating the nodule volume, maximum/average diameter, and isotropy directly from the fitted ellipsoid.

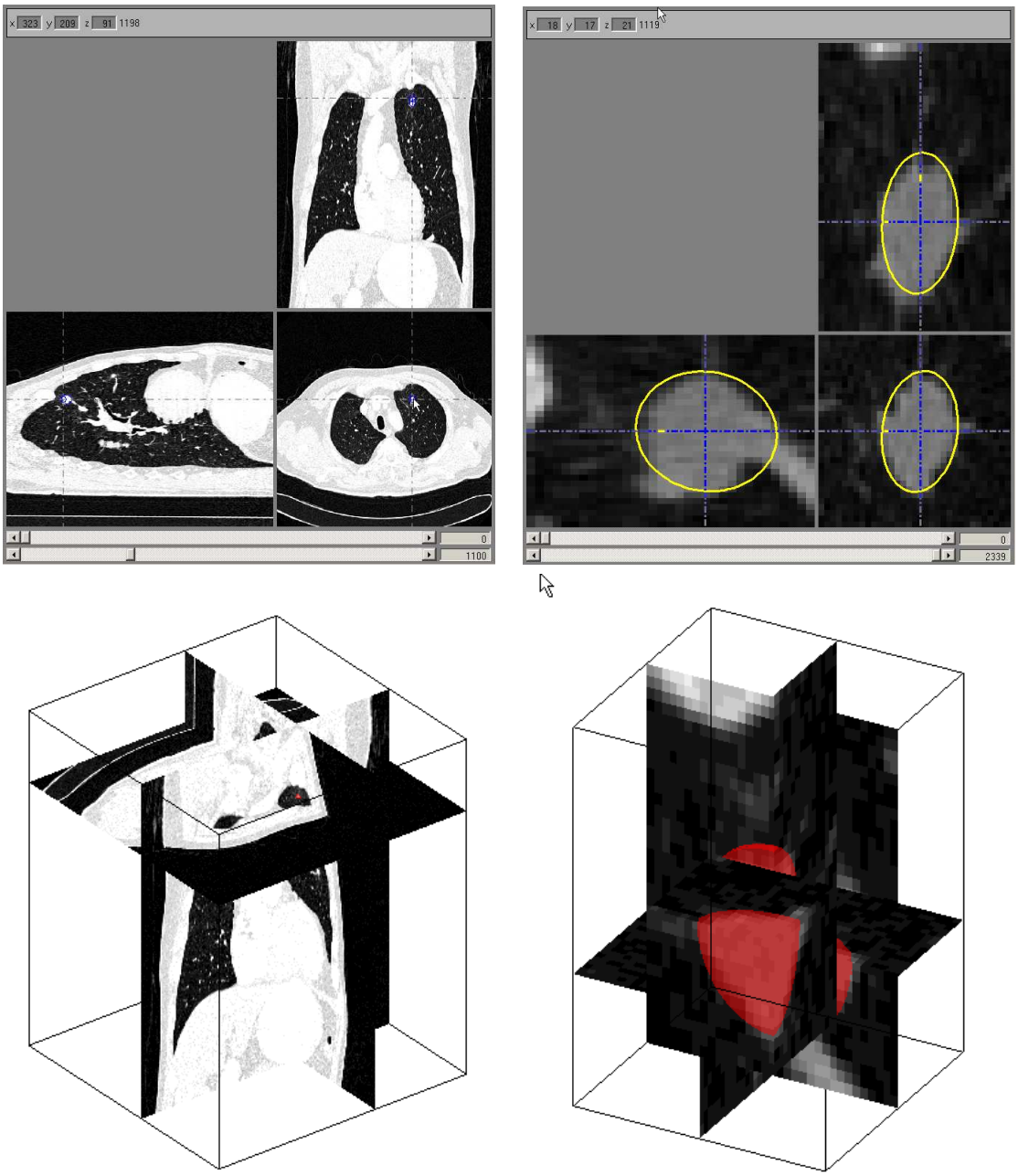

Figure 6: Quasi real-time nodule characterization and visualization. Three slices of the volume data read from dicom files can be viewed in 2D (top) and 3D (bottom) layouts. A mouse-click in the root view (top-left) initiates the nodule characterization process. After an average of 2 seconds, the process is completed and results in a zoom-up view of the nodule in the 2D (top-right) and 3D (bottom-right) layouts, as well as its volumetric measurements. The estimated nodule spread is visualized by yellow ellipses in the top-right figure and a red opaque ellipsoid in the bottom-right figure.

The nodule characterization system is validated by two sets of the large number of nodules as well as 1D and 2D synthetic data. The experimental results with the clinical chest HRCT data demonstrated a successful application of volumetric nodule characterization, providing robust estimation of 3D location and anisotropic spread, as well as the stable volumetric measurements, of the non-spherical pulmonary nodules. The quasi real-time system developed in this study also provides an efficient tumor visualization that can aid the tasks of radiologists. Such application for visualization is possible due to the ellipsoidal nature of our tumor characterization unlike other promising features such as fractal dimension analysis [17, 18].

As discussed in the introduction, the importance of accurately diagnosing the small and part- or non-solid (GGO) nodules has been revealed by recent clinical studies. Such clinical demands pose technical challenges since much higher characterization accuracy in both shape and volume is required for detecting the malignancy and for quantifying the related tumor growth-rate. Moreover, the voxel intensity distribution of the sub-solid nodules are much more irregular than the typical nodules targeted by the previous studies. Our experimental results suggest that the proposed model-based approach is a promising technique for segmenting and quantifying the volume of the non-solid nodules, with which the intensity thresholding-based segmentation may fail. More GGO cases, especially the part-solid nodules, should be further evaluated in future for deriving more clinically conclusive result.

One of the contributions of this work is the proposed estimation solution for the fully anisotropic Gaussian intensity model. The importance of considering the anisotropic covariance in the scale-space was also suggested by Lillholm et al. [39] in their image reconstruction analyses with various local features defined as combinations of the first and second order scale-space derivatives. Their results have direct implications to our problem since the second order derivatives (or Hessian matrix) are explicitly related to the covariance matrix [2, p.178][40].

The main technical strengths of our solution is its robustness against the effects of the margin-truncation (i.e., attachment to vessels and pleural surfaces) and the non-Gaussianity (i.e., part- and non-solid nodules) that are common in the pulmonary CT data or clinically significant. Such robustness is due to the nature of our framework consisting of i) the multi-scale joint Gaussian fitting and segmentation using only samples within the basin of attraction, ii) the divergence-based scale selection, and iii) the constraint least-squares covariance estimation. The robustness against the non-Gaussianity also supports our choice of the Gaussian intensity model. While such model is appropriate for small nodules due to the partial volume effect, it may not serve as an accurate model for large nodules whose intensity profile tends to resemble a

constant plateau or a step function. The scale-space approach used in our solution helps to fit a Gaussian function to such data by regularizing a step function into more Gaussian-like uni-modal signal. Moreover, the stability-based scale selection algorithm helps to absorb the modeling error by choosing the best fit regardless of such errors.

The proposed solutions provide volumetric measurements of target nodules which can be used for the differential diagnosis in the CAD application context. The advantage of our approach is three-folds. First, our solution inherits the robustness of our model estimation solution, resulting in a low intra- and inter-operator variability of the measurements. Second, the ellipsoidal formulation provides the type of measurements such as the average diameter and isotropy that are difficult to measure by conventional methods. Third, the robust solution for measuring the maximum nodule diameter can be related to the clinical RECIST scheme. The main issue of our approach is a bias due to the ellipsoidal approximation. The ellipsoidal segmentation is limited to an approximation of true tumor boundary. When the target tumor possesses irregular surface, the volumetric measurements by our method can be biased from the absolute value of the (unknown) ground-truth volume. While this issue can be well addressed by the previous segmentation-based approaches that explicitly account for the irregular surface structures and the boundary between the nodule and other structures (e.g., Kostis et al. [14]), the robustness of such approach has not been fully investigated. The proposed solution emphasizes the robustness over the ability to describe fine surface structure. In the context of the differential diagnosis, this may be a reasonable trade-off when, due to the robustness, the bias is unique to specific data, because such bias can be then canceled by differentiating a pair of volumes.

Our experimental results also indicated that most of the biased estimations were due to the small nodules with pleural attachments. In the nodule taxonomy introduced by Kostis et al. [14], our system performed well on the well-circumscribed, vascularized, and pleural tail nodules. Although many juxtapleural cases were also characterized correctly by our robust method, most of the failures were due to this type of nodules when they are small and heavily embedded into the surface. In such situation, the nodule center may become an unstable spatial local maximum, forcing the center/mean estimate to be drifted to a nearby non-target peak such as rib bones. This is an open issue of the proposed approach. Further improvement of the system performance on such case is clinically important since such peripheral nodules are found frequently in practice.

The issue of the estimation bias due to the ellipsoidal approximation can be solved by combining the proposed model-based approach with an additional non-parametric segmentation-based approach. The el-

lipsoidal approximation derived from the Gaussian fitted by our method can be used as the initial prior state, from which the finer boundary segmentation can be non-parametrically derived. Moreover, the intensity statistics can be sampled only within the ellipsoidally segmented nodule area, reducing the estimation bias. We have recently proposed such a non-parametric segmentation solution using 4D joint domain density mean shift analysis where the analysis bandwidth is directly derived from the fitted Gaussian [25]. Another natural continuation of this study is the extension of our framework for the automatic nodule detection problem. The most simple approach is to apply our nodule characterization solution from a set of markers distributed over the entire lung volume. This requires an intelligent sampling scheme and voting mechanism for realizing an efficient automatic detection solution, which remains as our future work.

Overall, our solution is generic and does not depends on semantics of the absolute CT values in the Hounsfield unit. The robustness, flexibility, and efficiency of the proposed framework, therefore, facilitates not only the pulmonary nodule applications in CT sought in this article but also various other applications in different imaging domains (e.g., PET scans) and different pathological and anatomical structures (e.g., polyps), involving with the analysis of blob-like geometrical structures. We plan to explore such other applications of our method in near future.

Acknowledgments

The authors wish to thank Visvanathan Ramesh from Siemens Corporate Research for stimulating discussions, Alok Gupta from CAD group, Siemens Medical Solutions, for his support and encouragement, and Jonathan Stoeckel from CAD group, Siemens Medical Solutions, for providing us the volume visualization tool and for his valuable technical supports. We also thank anonymous reviewers of this article for their thorough and insightful comments.

References

[1] T. Lindeberg, "Feature detection with automatic scale selection," *Int. J. Comput. Vision*, vol. 30, no. 2, pp. 79–116, 1998.

[2] B. Matei, "Heteroscedastic errors-in-variables models in computer vision," Ph.D. dissertation, Rutgers University, 2001.

[3] H. K. Weir et al., "Annual report to the nation on the status of cancer, 1975-2000," *Journal of the National Cancer Institute*, vol. 95, no. 17, pp. 1276–1299, 2003.

[4] J. P. Ko and D. P. Naidich, "Lung nodule detection and characterization with multislice CT," *Radiol. Clin. N. Am.*, vol. 41, pp. 575–597, 2003.

[5] T. Ohtsuka, H. Nomori, H. Horio, T. Naruke, and K. Suemasu, "Radiological examination for peripheral lung cancers and benign nodules less than 10 mm," *Lung Cancer*, vol. 42, pp. 291–296, 2003.

[6] F. Fischback, F. Knollmann, V. Griesshaber, T. Freund, E. Akkol, and R. Felix, "Detection of pulmonary nodules by multislice computed tomography: improved detection rate with reduced slice thickness," *Eur. Radiol.*, vol. 13, pp. 2378–2383, 2003.

[7] A. P. Reeves and W. J. Kostis, "Computer-aided diagnosis of small pulmonary nodules," *Seminars in Ultrasound, CT, and MRI*, vol. 21, no. 2, pp. 116–128, 2000.

[8] B. van Ginneken, B. M. ter Haar Romeny, and M. A. Viergever, "Computer-aided diagnosis in chest radiography: A survey," *IEEE Trans. Medical Imaging*, vol. 20, no. 12, pp. 1228–1241, 2001.

[9] M. S. Brown, M. F. McNitt-Gray, J. G. Goldin, R. D. Suh, J. W. Sayre, and D. R. Aberle, "Patient-specific models for lung nodule detection and surveillance in CT images," *IEEE Trans. Medical Imaging*, vol. 20, no. 12, pp. 1242–1250, 2001.

[10] Y. Lee, T. Hara, H. Fujita, S. Itoh, and T. Ishigaki, "Automated detection of pulmonary nodules in helical CT images based on an improved template-matching technique," *IEEE Trans. Medical Imaging*, vol. 20, no. 7, pp. 595–604, 2001.

[11] H. Takizawa, S. Yamamoto, T. Matsumoto, Y. Tateno, T. Iinuma, and M. Matsumoto, "Recognition of lung nodules from X-ray CT images using 3D markov random field models," in *Int. Conf. Pattern Recog.*, Quebec City, 2002.

[12] B. Zhao, G. Gamsu, M. S. Ginsberg, L. Jian, and L. H. Schwartz, "Automatic detection of small lung nodules on CT utilizing a local density maximum algorithm," *Journal of Applied Clinical Medical Physics*, vol. 4, no. 3, pp. 248–260, 2003.

[13] B. Zhao, D. Yankelevitz, A. Reeves, and C. Henschke, "Two-dimensional multi-criterion segmentation of pulmonary nodules on helical CT images," *IEEE Trans. Medical Imaging*, vol. 22, no. 10, pp. 1259–1274, 2003.

[14] W. J. Kostis, A. P. Reeves, D. F. Yankelevitz, and C. I. Henschke, "Three-dimensional segmentation and growth-rate estimation of small pulmonary nodules in helical CT images," *IEEE Trans. Medical Imaging*, vol. 22, no. 10, pp. 1259–1274, 2003.

[15] D. Wormanns, G. Kohl, E. Kotz, A. Marheine, F. Beyer, W. Heindel, and S. Diederich, "Volumetric measurements of pulmonary nodules at multi-row detector CT : in vivo reproducibility," *Eur. Radiol.*, vol. 14, no. 1, pp. 86–92, 2004.

[16] J. P. Ko, H. Rusinek, E. L. Jacobs, J. S. Babb, M. Betke, G. McGuinness, and D. P. Naidich, "Small pulmonary nodules: Volume measurement at chest CT - phantom study," *Radiology*, vol. 228, no. 3, pp. 864–870, 2003.

[17] Y. Kawata, N. Niki, H. Ohmatsu, M. Kusumoto, R. Kakinuma, K. Mori, H. Nishiyama, K. Eguchi, M. Kaneko, and N. Moriyama, "Computerized analysis of pulmonary nodules in topological and histogram feature spaces," in *Int. Conf. Pattern Recog.*, Barcelona, 2000.

[18] S. Kido, K. Kuriyama, M. Higashiyama, T. Kasugai, and C. Kuroda, "Fractal analysis of internal and peripheral textures of small peripheral bronchogenic carcinomas in thin-section computed tomography: Comparison of bronchioloalveolar cell carcinomas with nonbronchioloalveolar cell carcinomas," *Journal of Computer Assisted Tomography*, vol. 27, no. 1, pp. 56–61, 2003.

[19] D. Wormanns, M. Fiebich, M. Saidi, S. Diederich, and W. Heindel, "Automatic detection of pulmonary nodules at spiral CT : clinical application of a computer-aided diagnosis system," *Chest*, vol. 12, no. 1, pp. 1052–1057, 2002.

[20] M. Kass, A. Witkin, and D. Terzopoulos, "Snakes: Active contour models," *Int. J. Comput. Vision*, vol. 1, pp. 321–331, 1987.

[21] C. I. Henschke, D. F. Yankelevitz, R. Mirtcheva, G. McGuinness, D. McCauley, and O. S. Miettinen, "CT screening for lung cancer: frequency and significance of part-solid and non-solid nodules," *AJR Am. J. Roentgenol.*, vol. 178, no. 5, pp. 1053–1057, 2002.

[22] A. Witkin, "Scale-space filtering," in *Int. Joint. Conf. Artificial Intell.*, Karlsruhe, 1983, pp. 1019–1021.

[23] J. J. Koenderink, "The structure of images," *Biol. Cybern.*, vol. 50, pp. 363–370, 1984.

[24] D. Comaniciu and P. Meer, "Mean shift: A robust approach toward feature space analysis," *IEEE Trans. Pattern Anal. Machine Intell.*, vol. 24, no. 5, pp. 603–619, 2002.

[25] K. Okada, D. Comaniciu, and A. Krishnan, "Robust 3D segmentation of pulmonary nodules in multislice CT images," in *Medical Image Computing and Computer-Assisted Intervention*, Saint Malo, 2004.

[26] K. Fukunaga, *Statistical Pattern Recognition*. San Diego: Academic Press, 1990.

[27] P. J. Rousseeuw and A. M. Leroy, *Robust Regression and Outlier Detection*. New York: John Wiley, 1987.

[28] A. Bhalerao and R. Wilson, "Estimating local and global structure using a gaussian intensity model," in *Medical Image Understanding and Analysis*, Birmingham, 2001.

[29] P. Perona and J. Malik, "Scale-space and edge detection using anisotropic diffusion," *IEEE Trans. Pattern Anal. Machine Intell.*, vol. 12, no. 7, pp. 629–639, 1990.

[30] R. Manmatha and N. Srimal, "Scale space technique for word segmentation in handwritten documents," in *Int. Conf. Scale-Space Theories in Computer Vision*, 1999, pp. 22–33.

[31] M. J. Black, G. Sapiro, D. Marimont, and D. Heeger, "Robust anisotropic diffusion," *IEEE Trans. Image Processing*, vol. 7, no. 3, pp. 421–432, 1998.

[32] M. Nielsen, L. Florack, and R. Deriche, "Regularization, scale space, and edge detection filters," *J. Mathematical Imaging and Vision*, vol. 7, no. 4, pp. 291–307, 1997.

[33] D. Comaniciu, "An algorithm for data-driven bandwidth selection," *IEEE Trans. Pattern Anal. Machine Intell.*, vol. 25, no. 2, pp. 281–288, 2003.

[34] H. Hu, "Positive definite constrained least-squares estimation of matrices," *Linear Algebra and Its Applications*, vol. 229, pp. 167–174, 1995.

[35] G. H. Golub and C. F. van Loan, *Matrix Computations*. Baltimore: Johns Hopkins University Press, 1996.

[36] Y. Chen and J. E. McInroy, "Estimating symmetric, positive definite matrices in robotic control," in *IEEE Int. Conf. Robotics and Automation*, Washington D.C., 2002, pp. 4269–4274.

[37] S. van Huffel and J. Vandewalle, *The Total Least Squares Problem Computational Aspects and Analysis*. Philadelphia: SIAM, 1991.

[38] W. H. Press, S. A. Teukolsky, W. T. Vetterling, and B. P. Flannery, *Numerical Recipes in C*. Cambridge: Cambridge University Press, 1992.

[39] M. Lillholm, M. Nielsen, and L. D. Griffin, "Feature-based image analysis," *Int. J. Comput. Vision*, vol. 52, no. 2/3, pp. 73–95, 2003.

[40] Y. Kanazawa and K. Kanatani, "Do we really have to consider covariance matrices for image features?" in *Int. Conf. Computer Vision*, Vancouver, 2001, pp. 586–591.